HHS Public Access

Author manuscript

J Control Release. Author manuscript; available in PMC 2024 May 01.

Published in final edited form as:

J Control Release. 2023 May ; 357: 84–93. doi:10.1016/j.jconrel.2023.03.036.

STING agonist-loaded mesoporous manganese-silica nanoparticles for vaccine applications

Cheng Xu[a,b], **Hannah E. Dobson**[a,b], **Mengjie Yu**[c], **Wang Gong**[d], **Xiaoqi Sun**[a,b], **Kyung Soo Park**[b,e], **Andrew Kennedy**[f,g], **Xingwu Zhou**[a,b], **Jin Xu**[a,b], **Yao Xu**[a,b], **Andrew W. Tai**[f,g], **Yu Leo Lei**[d,h,i], **James J. Moon**[a,b,e,i,j,*]

[a]Department of Pharmaceutical Science, University of Michigan, Ann Arbor, MI 48109, USA

[b]Biointerfaces Institute, University of Michigan, Ann Arbor, MI 48109, USA

[c]Macromolecular Science and Engineering, University of Michigan, Ann Arbor, MI, USA

[d]Department of Periodontics and Oral Medicine, University of Michigan, Ann Arbor, MI, USA

[e]Department of Biomedical Engineering, University of Michigan, Ann Arbor, MI, USA

[f]Department of Internal Medicine, University of Michigan Medical School, Ann Arbor, MI, USA

[g]Department of Microbiology and Immunology, University of Michigan Medical School, Ann Arbor, MI, USA

[h]Department of Otolaryngology, University of Michigan, Ann Arbor, MI, USA

[i]Rogel Cancer Center, University of Michigan, Ann Arbor, MI, USA

[j]Department of Chemical Engineering, University of Michigan, Ann Arbor, MI, USA

Abstract

Cyclic dinucleotides (CDNs), as one type of Stimulator of Interferon Genes (STING) pathway agonist, have shown promising results for eliciting immune responses against cancer and viral infection. However, the suboptimal drug-like properties of conventional CDNs, including their short *in vivo* half-life and poor cellular permeability, compromise their therapeutic efficacy. In this study, we have developed a manganese-silica nanoplatform (MnO_x@HMSN) that enhances the adjuvant effects of CDN by achieving synergy with Mn^{2+} for vaccination against cancer and SARS-CoV-2. MnO_x@HMSN with large mesopores were efficiently co-loaded with CDN and peptide/protein antigens. MnO_x@HMSN(CDA) amplified the activation of the STING pathway and enhanced the production of type-I interferons and other proinflammatory cytokines from

*Corresponding author at: Department of Pharmaceutical Science, University of Michigan, Ann Arbor, MI 48109, USA. moonjj@med.umich.edu (J.J. Moon).

Credit author statement

C.X. and J.J.M. designed the experiments. C.X., H.E.D., M.Y. and X.S. contributed to the design of specific experiments. C.X. developed MnOx@HMSN(CDA + antigen) and soluble vaccines. C.X. and H.E.D. performed flow cytometry. C.X., and M.Y. performed nanoparticle synthesis and characterization. C.X., W.G. and Y.L.L. performed Western blot. C.X., K.S.P., A.K. and A.W.T. performed the *in vitro* pseudo-typed virus neutralization assay. C.X., X.Z., J.X. and Y.X. performed tumor monitoring and ELISPOT assay. C.X. and J.J.M. wrote the original draft, reviewed, and edited paper.

Appendix A. Supplementary data

Supplementary data to this article can be found online at https://doi.org/10.1016/j.jconrel.2023.03.036.

dendritic cells. MnO_x@HMSN(CDA) carrying cancer neoantigens elicited robust antitumor T-cell immunity with therapeutic efficacy in two different murine tumor models. Furthermore, MnO_x@HMSN(CDA) loaded with SARS-CoV-2 antigen achieved strong and durable (up to one year) humoral immune responses with neutralizing capability. These results demonstrate that MnO_x@HMSN(CDA) is a versatile nanoplatform for vaccine applications.

Keywords

Vaccine; Immunotherapy; STING agonist; Neoantigen; Mesoporous silica nanoparticles

1. Introduction

Promising achievements have been made in the field of cancer immunotherapy, including the development of immune checkpoint blockade therapy and tumor neoantigen-based cancer vaccines [1,2]. However, the therapeutic outcome of immunotherapies is limited by the highly immunosuppressive tumor microenvironments, inadequate induction of cancer-specific T-cells, and their poor infiltration into tumors [1,2]. Due to the crucial mediator functions in antitumor and antivirus immunity, the stimulator of interferon genes (STING) pathway has recently been recognized as a novel target for the development of cancer vaccines as well as viral vaccines, including the SARS-CoV-2 vaccine [3,4]. Acting as an innate immune danger sensor, cyclic GMP-AMP synthetase (cGAS) detects damage-associative double-stranded DNA in the cytosol, leading to activation of STING pathway and production of type I interferons and other proinflammatory cytokines [5]. Although recent preclinical studies on the delivery of cyclic dinucleotides (CDNs) have achieved promising anti-tumor outcomes, conventional CDNs have major limitations, including their short serum half-lives, rapid tissue clearance, and poor cellular permeability [6].

To address these limitations, several groups, including ours, have developed various types of nanoparticles (NPs) as vehicles for the delivery of STING agonists [7–12]. Among them, biodegradable mesoporous silica nanoparticles (MSNs) with excellent biocompatibility and good drug-loading capacity, have been demonstrated as an efficient nanocarrier for STING agonists for applications in cancer immunotherapy [7–9,13–15]. Furthermore, MSNs with large pores (4–10 nm) have been widely used for delivering peptides and proteins since MSNs have a relatively large loading capacity for macromolecules and allow for the prolonged release of cargo materials [16–18]. Interestingly, increasing attention has been paid to using metal ion Mn^{2+} to further improve the STING activation by strengthening the cGAMP[G(2′,5′)pA(3′,5′)]/STING binding affinity, thus lowering the detection limit of host immune cells to double-strand DNA or virus DNA by several orders of magnitude [19,20]. Studies, including one report from our group [21], have demonstrated the synergistic effects of CDN and Mn^{2+} for cancer immunotherapy [22–25].

Emerging evidence from clinical trials indicates that neoantigen-based vaccines enhance the therapeutic outcomes of several difficult-to-cure malignancies, such as melanoma, glioblastoma, and ovarian cancer [2,26]. It is reasonable to anticipate that concurrent delivery of both tumor neoantigen and adjuvant based on STING agonist and Mn^{2+} by one

multifunctional nanocarrier system may further enhance tumor-specific CD4+ and CD8+ T-cell responses, thus offering a more potent and safer strategy for the specific elimination of cancer cells [27,28]. Furthermore, the same nanocarrier system delivering STING agonist and Mn^{2+} may serve as a potent adjuvant for the induction of cellular and humoral immune responses against infectious pathogens [3,4]. Thus, it is desirable to develop an adjuvant platform that can be readily loaded with either cancer or microbial antigens for general vaccination applications.

In this work, we have developed manganese oxide-coated hollow MSN nanoparticles (MnO_x@HMSN) as a vaccine platform for the co-delivery of antigens (tumor or virus) with CDN and Mn^{2+} adjuvant. We show for the first time that MnO_x@HMSN co-delivering CDN and Mn^{2+} can be employed for vaccination against cancer as well as SARS-CoV-2. Notably, CDN and manganese ion released from MnO_x@HMSN significantly augmented STING activation, leading to robust production of type-I interferons and other proinflammatory cytokines. At the same time, CDNs and reactive oxygen species (ROS) from MnO_x@HMSN promoted the activation of dendritic cells (DCs), facilitating the subsequent uptake and cross-presentation of neoantigen peptides, leading to potent and durable neoantigen-specific $CD8^+$ T-cell response. Moreover, MnO_x@HMSN were efficiently loaded with CDN and receptor binding domain (RBD) of SRAS-CoV-2 and induced robust RBD-specific-IFN-γ^+ T cell response and long-lasting IgG antibodies in mice. Overall, based on its strong immunostimulatory capability to induce potent cellular and humoral immune responses as well as its versability, biocompatibility, and biodegradability, MnO_x@HMSN is an attractive platform for vaccine applications.

2. Materials & methods

2.1. Reagents and materials

All reagents were analytical or higher grade. Manganese (II) chloride tetrahydrate ($MnCl_2$•$4H_2O$), tetraethyl orthosilicate (TEOS), cetyltrimethylammonium chloride (CTAC), triethanolamine (TEA), (3-aminopropyl) triethoxysilane (APS) were purchased from Sigma-Aldrich (St. Louis, MO). Antigen peptides, including CT26 AH1 peptide SPSYVYHQF, and Adpgk mutant peptide CSSASMTNMELM were synthesized by Genemed Biotechnologies (Torrance, CA). CDA (bis-(3′−5′)-cyclic dimeric adenosine monophosphate) was purchased from Invitrogen (Waltham, MA). SARS-CoV-2 Spike RBD protein was purchased from Anaspec (Fremont, CA). All other reaction chemicals and reagents were purchased from Thermo Fisher Scientific (Fair Lawn, NJ).

2.2. Characterization

TEM images were obtained using a JEOL 1400-PLUS with 60 kV field emission. Nitrogen adsorption-desorption isotherms, surface areas, and pore size were measured at 77.3 K using a Quantachrome NovaWin2 system and determined by the BET (Brunauer–Emmett–Teller) method. Size and surface zeta potential analysis was performed using a Nano-ZS90 Zetasizer (Malvern Instruments Ltd.). The Mn content in MnO_x@HMSN and the release of Mn ions were measured by Perkin-Elmer Nexion 2000 Inductively-coupled plasma mass

spectrometry (ICP-MS). The percentages of $Mn^{2+/3+/4+}$ were measured by using a Rigaku XRD system. UV–vis spectra were recorded on Agilent Cary 60 spectrophotometer.

2.3. Synthesis of MnO_x@HMSN and loading of CDA and neoantigens

Biodegradable HMSN was synthesized in 3 steps as in the previous reports [16,17]: (1) preparing a dense silica core; (2) coating with large-pore-sized mesoporous shell in an oil–water biphase system; (3) removal of the dense silica core. Briefly, ethanol (35 mL), deionized water (5.0 mL), and ammonia (1.5 mL) were added into a glass beaker and mixed at 35 °C for 10 min, followed by the addition of TEOS (2 mL). After 1 h of robust shaking, dense silica NPs were obtained. Dense silica NPs were coated with a biodegradable mesoporous SiO_2 layer by adding 3 g of CTAC, 0.09 g of TEA, and 20 mL of water to 0.1 g of dense silica NPs in a round-bottom beaker, followed by adding 10 mL of TEOS in cyclohexane (5 *v*/v%) with gently stirring. The coating reaction was kept at 60 °C for 12 h. After the reaction, mesoporous SiO_2 layer-coated dense silica NPs were collected by centrifugation (8000 *g*, 10 min). The SiO_2 core was removed by incubation with 30 mL Na_2CO_3 solution (0.2 M) at 50 °C for 1 h. CTAC was removed by washing three times with HCl/ethanol solution. MnO_x@HMSN was obtained by a simple calcination method: HMSN in 10 mL water (10 mg/mL) was added with 10 mg of manganese (II) chloride tetrahydrate and 3 mL of ethanol, followed by bath sonication (50 Hz, 200 W) for 15 min [29]. The product was collected by centrifugation (8000 *g*, 10 min) and dried overnight in an oven at 80 °C. The mixture was then calcined at 300 °C for 2 h in the air. The final MnO_x@HMSN powder was washed three times with deionized water. And dried in an oven at 80 °C overnight. For the loading of CDA, the MnO_x@HMSN was surface modified with APS to introduce amine groups (MnO_x@HMSN-NH_2) [16]. The release profiles of CDA, Adpgk, and RBD proteins from the nanoplatform were measured in a Krebs–Henseleit solution (a body fluid simulating physiological buffer, without protein) at RT. Release of CDA and Adpgk was measured by LC-MS at MW of 702.8 (CDA) and 1027.2 (Adpgk). Release of RBD protein was measured by SDS-PAGE, followed by quantification of protein bands using Image J.

2.4. Cell lines

CT26 and MC38 cancer cells were obtained from the American Type Culture Collection (ATCC, Manassas, VA) and cultured at 37 °C and with 5% CO_2 in RPMI 1640 medium supplemented with 10% fetal bovine serum (FBS) and 1% penicillin/streptomycin. THP1 cells expressing $hSTING^{R232}$ (WT) were purchased and cultured according to the instructions from Invivogen. Cells were used for *in vitro* and *in vivo* experiments when they reached ~80% confluence.

2.5. In vitro evaluation of BMDCs activation, cytokine secretion, and STING activation

Mouse bone marrow-derived dendritic cells (BMDCs) were prepared as described previously [30]. BMDCs were seeded in 12-well plates at 0.5 million cells per well and incubated with various concentrations of free CDA, MnO_x@HMSN, or MnO_x@HMSN(CDA) for 24 h. Then, half of the cells were collected and stained with CD40, CD80, and CD86, by flow cytometric analysis on Aurora, Cytek Biosciences. The other half of BMDC cells were collected for Western blot-based analysis of P-TBK1,

t-TBK1, P-STING, P–P65, t-P65, and β-actin. The cell media were also collected for the measurement of cytokines (IFN-β, TNF-α, IL-12) by ELISA. To evaluate the STING activation in human monocyte cell line THP-1 cells expressing hSTING^{R232} (WT), we seeded THP-1 cells in 12-well plates at 0.5 million cells per well and incubated with various concentrations of free CDA, free Mn^{2+} ($MnCl_2$), MnO_x@HMSN, or MnO_x@HMSN(CDA). After 24 h, the luminescence signal from each well was measured by a plate reader according to the instructions from Invivogen. For measuring intracellular ROS, BMDCs were pretreated with 0.5 μg/mL of LPS, CDA, or MnO_x@HMSN(CDA) with or without 0.5 mM H_2O_2, followed by incubation with DCFDA (2′,7′-dichlorodihydrofluorescein diacetate, 5 μM) for 0.5 h. Afterwards, the cells were collected and measured for the fluorescence intensity of DCF (2′,7′-dichlorodihydrofluorescein, ex/em 485/535 nm) by flow cytometric analysis.

2.6. In vivo immunization and cancer immunotherapy study

All animal experiments were conducted in accordance with the approval by the Institutional Animal Care and Use Committee at the University of Michigan (Ann Arbor, MI). Female BALB/c or C57BL/6 mice (6–8 weeks old, Jackson Laboratories) were inoculated subcutaneously with CT26 or MC38 cells, respectively, on both sides of the flank. The left flank was inoculated with 0.5 million tumor cells as the primary tumor, while the right flank was inoculated with 0.1 million tumor cells as the distant tumor. Tumor size was measured and calculated based on the equation: volume = length × width^2 × 0.5. When the primary tumor volume reached ~60 mm^3, only the primary tumor was treated intratumorally (IT) with the indicated vaccine formulations. In the CT26 tumor model, the primary tumor was treated with the following groups. Group 1, PBS; Group 2, free CDA (5 μg) + Mn^{2+} (2 μg) + AH1 peptide (10 μg); Group 3, HMSN(CDA (5 μg) + AH1 peptide (10 μg)) + Mn^{2+} (2 μg); Group 4, MnO_x@HMSN(CDA 5 μg) (containing Mn^{2+} 2 μg) or; Group 5, MnO_x@HMSN(CDA (5 μg) + AH1 peptide (10 μg)) (containing Mn^{2+} 2 μg). In the MC38 tumor model, the primary tumor was treated with the following groups. Group 1, PBS; Group 2, free CDA (5 μg) + Adpgk peptide (10 μg) + Mn^{2+} (2 μg); Group 3, MnO_x@HMSN(CDA 5 μg) (containing Mn^{2+} 2 μg) or; Group 4, MnO_x@HMSN(CDA (5 μg) + Adpgk peptide (10 μg)) (containing Mn^{2+} 2 μg). The tumor volume was recorded every other day by caliper measurements.

For the analysis of neoantigen-specific CD8α$^+$ T-cells among peripheral blood mononuclear cells (PBMCs), submandibular bleeding was performed on the indicated days. After lysing red blood cells with ACK lysis buffer, a tetramer staining assay was performed using peptide-MHC-tetramer tagged with PE (H-2D^b-restricted ASMTNMELM (Adpgk), from NIH Tetramer Core Facility). For the analysis of T-cells, NK cells, and DCs in the tumor microenvironment, tissues were cut into small pieces and passed through a 70 μm cell strainer. Then the cell suspensions were washed and stained with the following reagents: CD3-APC, CD4-BV605, CD8α-Pac Blue, Adpgk-tetramer-PE, CD45-AF700, CD11c-BV650, CD11b-PerCp-Cy5.5, MHC-II-BV510, CD80-PE-Cy5, F4/80-PE-Cy7, Ly6C-BV711, and NK1.1-BV750. After antibody staining, cells were analyzed by flow cytometric analysis.

2.7. In vivo anti-viral immunization study

To analyze the lymph node distribution of CDN delivered by MnO_x@HMSN, Cy7-conjugated CDG was loaded into MnO_x@HMSN as described above for CDA-loaded MnO_x@HMSN. To quantify the lymph node distribution, we injected free Cy7-CDN or MnO_x@HMSN(Cy7-CDN) subcutaneously into the tail base of BALB/c mice. After 24 h, mice were euthanized, and inguinal lymph nodes were collected, and the average fluorescence signal was measured by the IVIS system.

To evaluate the anti-viral immune responses elicited by the MnO_x@HMSN system, we loaded SARS-CoV-2 RBD protein into MnO_x@HMSN. In brief, 5 μg RBD protein was mixed with 1 mg MnO_x@HMSN(CDA) for 0.5 h at RT. After washing 3 times with PBS, the pellet and supernatant were collected and analyzed for the loading of RBD in MnO_x@HMSN(CDA) by sodium dodecyl-sulfate polyacrylamide gel electrophoresis (SDS-PAGE), followed by Commassie blue staining. For the *in vivo* vaccination study, 6–8 weeks old female BALB/c mice (Jackson Laboratories) were subcutaneously immunized with free CDA (5 μg) + RBD protein (0.5 μg) + Mn^{2+} (2 μg) or MnO_x@HMSN(CDA + RBD) (contain 5 μg CDA and 0.5 μg RBD) at the tail base. An equivalent dose of CDA and RBD was injected as a boost immunization after 2 weeks of the first immunization. The peripheral blood was collected at designed time points, and anti-RBD lgG titer in serum was measured by ELISA. An IFN-γ ELISPOT assay was performed on isolated PBMCs with RBD protein 2 weeks after the second immunization. To study viral neutralization capacity, we performed a pseudo typed-virus luminescence neutralization study using serum samples collected on week 6.

2.8. Statistical analysis

Sample sizes were chosen based on preliminary data from pilot experiments and previously published reports. All animal studies were performed after randomization. Data were analyzed by one-way or two-way analysis of variance (ANOVA), followed by Tukey's HSD multiple comparison *post hoc* test with Prism 9.4 (GraphPad Software). Data were normally distributed and *P*-values < 0.05 were considered statistically significant. Statistical significance was denoted with $*P < 0.05$, $**P < 0.01$, $***P < 0.001$, or $****P < 0.0001$.

3. Results and discussion

3.1. Synthesis and characterizations of MnO_x@HMSN(CDA)

We have synthesized a MnO_x@HMSN nanoplatform to enhance the adjuvant effects of CDNs for vaccine applications in cancer and infectious diseases (Fig. 1). In particular, we have employed CDA as a prototypical CDN. We synthesized biodegradable hollow mesoporous silica nanoparticles (HMSN) with a large pore size by a water-oil biphase system as previously reported [16,17]. We then coated the surface of HMSN with small manganese oxide (MnO_x) nanoparticles by a simple thermal calcination process [29]. The resulting MnO_x@HMSN nanoparticles were surface-modified with amine and loaded simultaneously with CDA and antigen peptides/proteins. In this study, we examined the antitumor immune response of MnO_x@HMSN(CDA) carrying tumor neoantigens in the setting of cancer immunotherapy. Moreover, to demonstrate versatility of the vaccine

platform, we evaluated MnO_x@HMSN(CDA) carrying SARS-CoV-2 antigen as a potential COVID-19 vaccine and showed the induction of cellular and humoral immune responses in mice (Fig. 1).

The morphology and structure of HMSN and MnO_x@HMSN were visualized by TEM (Fig. 2a–b). HMSN exhibited a uniform, spherical, highly porous dendritic morphology with an average diameter of 190 nm ± 22 nm and a polydispersity index (PDI) of 0.24, as measured by dynamic light scattering (DLS) (Fig. 2d). After surface coating with ultrasmall manganese oxide nanoparticles (MnO_x, 2–4 nm), followed by a surfactant-free, calcination step, the average size of MnO_x@HMSN increased slightly to 199 nm ± 28 nm with a PDI of 0.29 (Fig. 2b–d). The average pore size of MnO_x@HMSN was 3–10 nm, as measured by the nitrogen adsorption-desorption test (Fig. 2e); large surface mesopores of MnO_x@HMSN are advantageous for loading and delivery of biological macromolecules [16,17]. The average Mn content in MnO_x@HMSN was 4.7%, and 53.2% of Mn in the MnO_x was Mn^{2+} as analyzed by ICP-MS and X-ray photoelectron spectroscopy (XPS) (Fig. 2f and Fig. S1a).

The release of manganese ions from MnO_x@HMSN was measured in PBS (pH = 7.4), PBS (pH = 6.0), or PBS (pH = 6.0) with 10 mM glutathione (GSH) at RT. We observed an accelerated release of manganese ions from MnO_x@HMSN incubated in PBS (pH = 6.0) with 10 mM GSH, compared with that in PBS (pH = 7.4) or PBS (pH = 6.0) (Fig. 2g). These results suggest that Mn^{2+} would be released more readily in tumors with a slightly acidic and GSH-rich environment, compared with normal tissues [31]. The surface zeta potential of MnO_x@HMSN-NH_2 (APS-conjugated MnO_x@HMSN) was 8.6 ± 1.2 mV and became negative at −5.2 ± 1.4 mV for MnO_x@HMSN(CDA) after loading CDA by electrostatic interaction (Fig. 2h). The average loading capacity of CDA in MnO_x@HMSN was 12.1 ± 2.6 μg per 1 mg MnO_x@HMSN (Fig. 2i and Fig. S1b–d), and ~ 56% of CDA and ~ 35% of antigens initially loaded in MnO_x@HMSN were released over 24 h in Krebs–Henseleit solution (Fig. S1g–i).

3.2. In vitro evaluation of STING activation and IFN-I response

We examined the activation of cGAS-STING-IFN-I pathway by MnO_x@HMSN(CDA) using both human monocyte-like THP-1 cells and mouse BMDCs. As shown in Fig. 3a, THP1-mSTING cells exhibited significantly higher STING activation after treatment with MnO_x@HMSN(CDA) across three different doses of CDA at 0.1, 0.25, and 0.5 μg/mL (with Mn^{2+} concentration of 0.7, 1.4, and 2.8 μg/mL, respectively), compared with either an equivalent dose of free CDA, an equivalent Mn^{2+} dose of nanocarriers without CDA, or free CDA (0.5 μg/mL) + Mn^{2+} (2.8 μg/mL) (Fig. 3a). In addition, MnO_x@HMSN(CDA) across three different doses of CDA at 0.1, 0.25, and 0.5 μg/mL induced significantly higher secretion of IFN-β, TNF-α, and IL-2 from BMDCs, compared with either an equivalent dose of free CDA, an equivalent Mn^{2+} dose of nanocarriers without CDA, or free CDA (0.5 μg/mL) + Mn^{2+} (2.8 μg/mL) (Fig. 3b–d). We did not observe any noticeable cytotoxicity after MnO_x@HMSN(CDA) treatment (Fig. S2a).

To understand the mechanism of STING activation by MnO_x@HMSN (CDA), we examined the downstream signaling of the cGAS-STING-IFN-I pathway after treatment with either free CDA, MnO_x@HMSN, or MnO_x@HMSN(CDA) in BMDCs. As shown in Fig. 3e,

MnO_x@HMSN treatment alone induced robust phosphorylation of STING as well as p65 (both are important transcription factors in the downstream IFN-I pathway [19]), suggesting that manganese ion may induce the activation of the cGAS-STING-IFN-I pathway. Notably, treatment with MnO_x@HMSN(CDA) further enhanced the level of phosphorylated STING and phosphorylated p65, suggesting synergistic activation of the cGAS-STING-IFN-I pathway when CDA is delivered *via* MnO_x@HMSN.

Moreover, treatment with MnO_x@HMSN(CDA) led to higher upregulation of CD80 and CD86 costimulatory markers on BMDCs, compared with free CDA + Mn^{2+} treatment (Fig. 3g–h), indicating DC activation and maturation by MnO_x@HMSN(CDA). We also examined the intracellular level of ROS in BMDCs treated with MnO_x@HMSN(CDA). Treatment with MnO_x@HMSN(CDA) led to higher DCF fluorescence (a ROS indicator) in BMDCs, compared with free CDA treatment (Fig. 3i), potentially due to the high valence of Mn ion ($Mn^{3+/4+}$) in MnO_x@HMSN (Fig. 2e and S2b) [12]. Several studies have demonstrated that Mn^{2+} can generate cytotoxic hydroxyl radicals (•OH) through Fenton-like reactions for potential chemodynamic therapy relying on the endogenous H_2O_2 inside of tumors [31,32]. Indeed, with the addition of 5 mM H_2O_2, the DCF fluorescence further doubled in MnO_x@HMSN(CDA) treated cells, indicating higher level of cellular ROS in the presence of H_2O_2 (Fig. 3i). Notably, we have previously reported that ROS-producing nanocarriers can alkalize the endolysosomes of DCs, leading to the protection of antigen peptides/proteins from endolysosomal degradation and enhanced antigen cross-presentation to T-cells [27]. Taken together, these results show that MnO_x@HMSN (CDA) induces robust STING activation and activates DCs *via* multiple mechanisms of action, suggesting MnO_x@HMSN(CDA) as a potential platform to elicit T-cell responses.

3.3. In vivo therapeutic study in CT26 and MC38 tumor models

We compared *in vivo* tissue retention of CDN formulated either as a free solution or loaded into MnO_x@HMSN. BABL/c mice were inoculated with 3×10^5 of CT26 tumor cells at SC flank, and after 10 days, we administered 10 μg of Cy7-tagged CDN either as free form (free Cy7-CDN) or MnO_x@HMSN(Cy7-CDN) *via* IT injection to CT26 tumors, followed by visualization by IVIS imaging. Within 24 h of injection, most Cy7-CDN was cleared from the tumor tissues, with only 14% of the initial fluorescence signal of Cy7-CDN detected in tumor tissues (Fig. 4a–b). In contrast, tumor tissues administered with MnO_x@HMSN(Cy7-CDN) still retained ~60% of the initial fluorescence signal of Cy7-CDN after 24 h, which was 4.4-fold higher than that of the free Cy7-CDN group ($P < 0.0001$, Fig. 4a–b). Even after 96 and 144 h, tumor tissues injected with MnO_x@HMSN(Cy7-CDN) retained 9.3-fold and 10.1-fold higher fluorescence signal, respectively, compared with soluble Cy7-CDN ($P < 0.01$ for 96 h for Fig. 4a–b), indicating prolonged tissue retention of MnO_x@HMSN(Cy7-CDN).

We next assessed the *in vivo* therapeutic efficacy of MnO_x@HMSN co-loaded with CDA and tumor antigens in CT26 tumor-bearing mice. MnO_x@HMSN(CDA) was simply admixed and incubated with AH1 peptide for 1 h at RT, and we observed efficient loading of AH1 onto MnO_x@HMSN(CDA) (~9 μg peptide/1 mg MnO_x@HMSN(CDA), Fig. S1b). The resulting MnO_x@HMSN(CDA + AH1) was evaluated for its therapeutic efficacy in a

bilateral two-tumor model. BALB/c mice were inoculated with 3×10^5 CT26 cells on the left side (primary) of the flanks and 1×10^5 CT26 cells on the right side (distant) of the flanks on day 0. After 8 and 15 days of tumor inoculation, we administered vaccines IT into the primary (left) tumors only, while the distant (right) tumors were left untreated (Fig. 4c). We first examined the induction of AH1 antigen-specific $CD8\alpha^+$ T-cells among PBMCs. Mice treated with soluble vaccine composed of CDA, AH1 peptide, and Mn^{2+} induced an average of 1.5% AH1-specific $CD8\alpha^+$ T-cells among $CD8\alpha^+$ T-cells on day 22 (*i.e.*, 7 days after the boost injection) (Fig. 4d). In contrast, mice treated with MnO_x@HMSN(CDA + AH1) elicited 7.2% AH1-specific $CD8\alpha^+$ T-cells, which was 3.2-fold higher than the soluble vaccine group ($P < 0.01$), and 2.6-fold higher than the HMSN(CDA + AH1) admix with Mn^{2+} group ($P < 0.01$) (Fig. 4d). Mice in the soluble vaccine group exhibited rapid growth of both primary and distant tumors (Fig. 4e–f). In stark contrast, MnO_x@HMSN(CDA + AH1) treatment resulted in significantly improved antitumor effects against both primary and distant tumors, compared with all other control groups, including soluble CDA + AH1 + Mn^{2+}, HMSN(CDA + AH1) + Mn^{2+}, and MnO_x@HMSN(CDA) (Fig. 4e–f). These results demonstrate strong local and abscopal antitumor effects of MnO_x@HMSN co-loaded with CDA and antigen.

Next, we investigated the antitumor therapeutic effects of MnO_x@HMSN(CDA) carrying a tumor neoantigen. MnO_x@HMSN(CDA) was admixed and incubated with Adpgk peptide (a neoantigen derived from MC38 colon carcinoma [28]) for 1 h at RT, leading to efficient loading of Adpgk onto MnO_x@HMSN(CDA) (~10 μg peptide/ 1 mg MnO_x@HMSN(CDA) (Fig. S1b). The resulting MnO_x@HMSN(CDA + Adpgk) was evaluated in an MC38 bilateral tumor model. C57BL/6 mice were inoculated with 5×10^5 MC38 cells on the left side (primary) of the flanks and 2×10^5 MC38 cells on the right side (distant) of the flanks on day 0. After 12 and 20 days of tumor inoculation, vaccine formulations were administered IT in the primary (left) tumors only, while the distant (right) tumors were left untreated (Fig. 4g). We first examined the induction of Adpgk-specific $CD8\alpha^+$ T-cells among PBMCs. Mice treated with MnO_x@HMSN(CDA + Adpgk) induced an average of 8.8% Adpgk-specific $CD8\alpha^+$ T-cells among $CD8\alpha^+$ T-cells on day 27 (*i.e.*, 7 days after the boost injection), which was 2.8-fold ($P < 0.01$) and 4.9-fold ($P < 0.05$) higher than that in MnO_x@HMSN(CDA) and soluble CDA + Adpgk + Mn^{2+} treated group, respectively (Fig. 4h). In line with these results, MnO_x@HMSN(CDA + Adpgk) treatment exerted the most robust antitumor efficacy among the comparison groups, leading to significantly enhanced antitumor effects against both the primary and distant tumors (Fig. 4i, j). Taken together, these results show that the MnO_x@HMSN nanoplatform extended the *in vivo* retention of CDA, and when co-loaded with tumor antigens, MnO_x@HMSN(CDA + peptide) elicited robust antigen-specific T-cells response with strong antitumor effects against both local and untreated distal tumors.

3.4. The immunomodulation effects in the tumor microenvironment

We next examined the antitumor immune response elicited by MnO_x@HMSN(CDA + Adpgk) treatment in the tumor microenvironment (TME) (Fig. 5). IT treatment with MnO_x@HMSN(CDA + Adpgk) led to significantly higher intratumoral infiltration of total $CD3^+$ T-cells and $CD8^+$ cytotoxic T-cells on day 7 after boost immunization, compared

with soluble CDA + Adpgk + Mn^{2+} ($P < 0.05$, Fig. 5a, c–d). We observed the most robust neoantigen-specific $CD8^+$ T-cell response for the MnO_x@HMSN(CDA + Adpgk) group, which induced 3.0-fold ($P < 0.05$) and 7.7-fold ($P < 0.01$) higher frequency of Adpgk-specific $CD8^+$ T cells, compared with soluble CDA + Adpgk + Mn^{2+} group and MnO_x@HMSN(CDA) without antigen on day 27 (Fig. 5b, e). Other than these, there were no significant changes among B cells, DCs, NK cells, monocytes, and $CD4^+$ T-cells for the 4 treatment groups (Fig. 5f) except for a slight decrease in the frequency of macrophages for the MnO_x@HMSN (CDA + Adpgk) group. Taken together, the TME analysis results showed that MnO_x@HMSN (CDA + Adpgk) treatment turned the local TME into more "inflamed" TME characterized by tumor-infiltrating antigen-specific cytotoxic CD8+ T-cells.

3.5. MnO_x@HMSN(CDA + RBD) as a potential COVID-19 vaccine

The coronavirus disease of 2019 (COVID-19) caused by SARS-CoV-2 viral infection caused more than 6 million deaths [33]. The spike RBD is the key binding interface that SARS-CoV-2 virus uses to initiate membrane fusion [34]. Having shown strong immunostimulatory properties of MnO_x@HMSN(CDA), we examined whether MnO_x@HMSN(CDA) with large surface mesopores can be loaded with recombinant RBD protein (28 kDa) and serve as a platform for vaccination against SARS-CoV-2. MnO_x@HMSN(CDA) was admixed and incubated with RBD protein for 1 h at RT, leading to efficient loading of RBD onto MnO_x@HMSN(CDA). Up to 5 μg RBD protein was incorporated per 1 mg MnO_x@HMSN, as shown by SDS-PAGE and Coomassie staining (Fig. 6a).

We examined lymphatic drainage of the vaccine nanoparticles after subcutaneous (SC) administration. Free Cy7-CDN + RBD or MnO_x@HMSN(Cy7-CDN + RBD) were administered SC, and inguinal lymph nodes were harvested after 6 h or 24 h, followed by quantification of the Cy7-CDN fluorescence signal by the IVIS imaging system. We observed significantly higher fluorescence signal in inguinal lymph nodes after vaccination with MnO_x@HMSN(Cy7-CDN + RBD), compared with Cy-CDN + RBD, at both 6 h and 24 h post-injection time points (Fig. 6b–c). These results showed that MnO_x@HMSN(Cy7-CDN + RBD) promoted lymphatic draining of CDN and its tissue retention in local lymph nodes.

Lastly, to investigate its potential as a COVID-19 vaccine, we gave a prime and a boost SC vaccination with MnO_x@HMSN(CDA + RBD) (2 weeks interval) in BALB/c mice, and cellular and humoral immune responses were examined at various time points (Fig. 6d). The SARS-CoV-2 RBD protein-specific T-cell response was tested using IFN-γ ELISPOT assay performed on PBMCs harvested on week 4 (Fig. 6e–f). The number of IFN-γ-secreting RBD-specific T-cells in the MnO_x@HMSN(CDA + RBD) treated group was almost 100-fold higher than the number in the soluble CDA + RBD + Mn^{2+} group (Fig. 6e–f). Humoral RBD-specific IgG response was also monitored after the prime immunization as shown in Fig. 6g. Remarkably, from 2 weeks after boost immunization (week 6) throughout 1 year (week 52), MnO_x@HMSN(CDA + RBD) vaccinated achieved over 50-fold higher RBD-specific serum IgG titers, compared with the soluble CDA + RBD + Mn^{2+} group ($P < 0.0001$, Fig. 6g). Furthermore, consistent with the IgG titer results, the sera from

MnO_x@HMSN(CDA + RBD) treatment group (from week 6) exhibited significantly higher efficiency in neutralization of pseudo-type virus *in vitro* ($P < 0.05$, Fig. 6h). Taken together, MnO_x@HMSN nanoplatform co-loaded with CDA and RBD elicited strong humoral and cellular immune responses against SARS-CoV-2, demonstrating its great potential as a vaccine platform.

4. Conclusions

In summary, we have developed a biocompatible, versatile, and Mn^{2+}-containing nanoplatform MnO_x@HMSN to amplify the adjuvant effects of CDA for vaccination against cancer or infectious pathogens. MnO_x@HMSN with large mesoporous surface can efficiently co-load CDA with tumor or viral antigens and prolong *in vivo* retention of vaccine components. As a result, MnO_x@HMSN(CDA) showed improved activation of the STING pathway and robust antitumor efficacy. Furthermore, MnO_x@HMSN(CDA + RBD) exhibited enhanced cellular immunity and greatly prolonged antiviral humoral immunity, compared with soluble CDA + RBD + Mn^{2+} vaccine. Those results indicate that MnO_x@HMSN is a powerful nanoplatform for improving the efficacy of CDN-based vaccines.

Supplementary Material

Refer to Web version on PubMed Central for supplementary material.

Acknowledgements

This work was supported in part by NIH (R01DE030691, R01DE031951, R01DE026728, R01DK125087, R01CA271799, R01NS122536, U01CA210152, P30CA046592). We acknowledge the NIH Tetramer Core Facility (contract HHSN272201300006C) for provision of MHC-I tetramers.

Declaration of Competing Interest

J.J.M. declares financial interests as board membership, a paid consultant, research funding, and/or equity holder in EVOQ Therapeutics, Saros Therapeutics, and Intrinsic Medicine.

Data availability

Data will be made available on request.

References

[1]. Couzin-Frankel J, Cancer immunotherapy, Science 342 (2013) 1432–1433. [PubMed: 24357284]

[2]. Aikins ME, Xu C, Moon JJ, Engineered nanoparticles for cancer vaccination and immunotherapy, Acc. Chem. Res 53 (2020) 2094–2105. [PubMed: 33017150]

[3]. Wu J, Zhao L, Han B, Hu H, Zhang B, Li W, Chen Y, Li Y, A novel STING agonist for cancer immunotherapy and a SARS-CoV-2 vaccine adjuvant, Chem. Commun 57 (2021) 504–507.

[4]. Zhou J, Ventura CJ, Fang RH, Zhang L, Nanodelivery of STING agonists against cancer and infectious diseases, Mol. Asp. Med 101007 (2021).

[5]. Sun L, Wu J, Du F, Chen X, Chen ZJ, Cyclic GMP-AMP synthase is a cytosolic DNA sensor that activates the type I interferon pathway, Science 339 (2013) 786–791. [PubMed: 23258413]

[6]. Meric-Bernstam F, Sandhu SK, Hamid O, Spreafico A, Kasper S, Dummer R, Shimizu T, Steeghs N, Lewis N, Talluto CC, Dolan S, Bean A, Brown R, Trujillo D, Nair N, Luke JJ, Phase Ib study

of MIW815 (ADU-S100) in combination with spartalizumab (PDR001) in patients (pts) with advanced/metastatic solid tumors or lymphomas, J. Clin. Oncol 37 (2019) 2507.

[7]. Park KS, Xu C, Sun X, Louttit C, Moon JJ, Improving STING agonist delivery for cancer immunotherapy using biodegradable mesoporous silica nanoparticles, Adv. Therap 3 (2020) 2000130.

[8]. Bielecki PA, Lorkowski ME, Becicka WM, Atukorale PU, Moon TJ, Zhang Y, Wiese M, Covarrubias G, Ravichandran S, Karathanasis E, Immunostimulatory silica nanoparticle boosts innate immunity in brain tumors, Nanoscale Horiz. 6 (2021) 156–157. [PubMed: 33400743]

[9]. Chen Y, Li Xu, Tang T, Chen C, Zheng Q, Liu T, Mou C, Wu C, Wu S, STING activator c-di-GMP-loaded mesoporous silica nanoparticles enhance immunotherapy against breast cancer, ACS Appl. Mater. Interfaces 12 (2020) 56741–56752. [PubMed: 33305564]

[10]. Chen C, Tong Y, Zheng Y, Shi Y, Chen Z, Li J, Liu X, Zhang D, Yang H, Cytosolic delivery of thiolated Mn-cGAMP nanovaccine to enhance the antitumor immune response, Small 17 (2020) 2006970.

[11]. Li J, Ren H, Qiu Q, Yang X, Zhang J, Zhang C, Sun B, Lovell JF, Zhang Y, Manganese coordination micelles that activate stimulator of interferon genes and capture in situ tumor antigens for Cancer Metalloimmunotherapy, ACS Nano 16 (2022) 16909–16923. [PubMed: 36200692]

[12]. Lu Q, Chen R, Du S, Chen C, Pan Y, Luan X, Yang J, Zeng F, He B, Han X, Song Y, Activation of the cGAS-STING pathway combined with CRISPR-Cas9 gene editing triggering long-term immunotherapy, Biomaterials 291 (2022), 121871. [PubMed: 36323073]

[13]. Becicka WM, Bielecki PA, Lorkowski ME, Moon TJ, Zhang Y, Atukorale PU, Covarrubias G, Karathanasis E, The effect of PEGylation on the efficacy and uptake of an immunostimulatory nanoparticle in the tumor immune microenvironment, Nanoscale Adv. 3 (2021) 4961–4972. [PubMed: 34485818]

[14]. Zhuang J, Holay M, Park JH, Fang RH, Zhang J, Zhang L, Nanoparticle delivery of immunostimulatory agents for cancer immunotherapy, Theranostics. 9 (2019) 7826–7848. [PubMed: 31695803]

[15]. Sun Z, Wang Z, Wang T, Wang J, Zhang H, Li Z, Wang S, Sheng F, Yu J, Hou Y, Biodegradable MnO-based nanoparticles with engineering surface for tumor therapy: simultaneous Fenton-like ion delivery and immune activation, ACS Nano 16 (2022) 11862–11875. [PubMed: 35925671]

[16]. Xu C, Nam J, Hong H, Xu Y, Moon JJ, Positron emission tomography-guided photodynamic therapy with biodegradable mesoporous silica nanoparticles for personalized cancer immunotherapy, ACS Nano 13 (2019) 12148–12161. [PubMed: 31556987]

[17]. Kong M, Tang J, Qiao Q, Wu T, Qi Y, Tan S, Gao X, Zhang Z, Biodegradable hollow mesoporous silica nanoparticles for regulating tumor microenvironment and enhancing antitumor efficiency, Theranostics 7 (2017) 3276–3292. [PubMed: 28900509]

[18]. Xu C, Chen F, Valdovinos HF, Jiang D, Goel S, Yu B, Sun H, Barnhart TE, Moon JJ, Cai W, Biomaterials 165 (2018) 56–65. [PubMed: 29501970]

[19]. Wang C, Guan Y, Lv M, Zhang R, Guo Z, Wei X, Du X, Yang J, Li T, Wan Y, Su X, Huang X, Jiang Z, Manganese increases the sensitivity of the cGAS-STING pathway for double-stranded DNA and is required for the host defense against DNA viruses, Immunity 48 (2018) 675–687. [PubMed: 29653696]

[20]. Lv M, Chen M, Zhang R, Zhang W, Wang C, Zhang Y, Wei X, Guan Y, Liu J, Feng K, Jing M, Wang X, Liu Y, Mei Q, Han W, Jiang Z, Manganese is critical for antitumor immune responses via cGAS-STING and improves the efficacy of clinical immunotherapy, Cell Res. 30 (2020) 966–979. [PubMed: 32839553]

[21]. Sun X, Zhang Y, Li J, Park KS, Han K, Zhou X, Xu Y, Nam J, Xu J, Shi X, Lei YL, Moon JJ, Amplifying STING activation by cyclic dinucleotide–manganese particles for local and systemic cancer metalloimmunotherapy, Nat. Nanotechnol 16 (2021) 1260–1270. [PubMed: 34594005]

[22]. Song W, Song S, Kuang J, Yang H, Yu T, Yang F, Wan T, Xu Y, Wei S, Li M, Xiong Y, Zhou Y, Qiu W, Activating innate immunity by a STING signal amplifier for local and systemic immunotherapy, ACS Nano 16 (2022) 15977–15993. [PubMed: 36190834]

[23]. Hou L, Tian C, Yan Y, Zhang L, Zhang H, Zhang Z, Manganese-based nanoactivator optimizes cancer immunotherapy via enhancing innate immunity, ACS Nano 14 (2020) 3927–3940. [PubMed: 32298077]

[24]. Gao M, Xie Y, Lei K, Zhao Y, Kurum A, Herck SV, Guo Y, Hu X, Tang L, A manganese phosphate nanocluster activates the cGAS-STING pathway for enhanced cancer immunotherapy, Adv. Therap 4 (2021) 2100065.

[25]. Yang X, Yang Y, Bian J, Wei J, Wang Z, Zhou Z, Li Z, Sun M, Converting primary tumor towards an in situ STING-activating vaccine via a biomimetic nanoplatform against recurrent and metastatic tumors, Nano Today 38 (2021), 101109.

[26]. Schumacher TN, Schreiber RD, Neoantigens in cancer immunotherapy, Science 348 (2015) 69–74. [PubMed: 25838375]

[27]. Xu C, Hong H, Lee Y, Park KS, Sun M, Wang T, Aikins ME, Xu Y, Moon JJ, Efficient lymph node-targeted delivery of personalized cancer vaccines with reactive oxygen species-inducing reduced graphene oxide nanosheets, ACS Nano 14 (2020) 13268–13278. [PubMed: 32902245]

[28]. Kuai R, Ochyl LJ, Bahjat KS, Schwendeman A, Moon JJ, Designer vaccine nanodiscs for personalized cancer immunotherapy, Nat. Mater 16 (2017) 489–496. [PubMed: 28024156]

[29]. Du W, Liu T, Xue F, Chen Y, Chen Q, Luo Y, Cai X, Ma M, Chen H, Confined nanoparticles growth within hollow mesoporous nanoreactors for highly efficient MRI-guided photodynamic therapy, J. Chem. Eng 379 (2020), 122251.

[30]. Lutz MB, Kukutsch N, Ogilvie ALJ, Rößner S, Koch F, Romani N, Schuler G, An advanced culture method for generating large quantities of highly pure dendritic cells from mouse bone marrow, J. Immunol. Methods 223 (1999) 77–92. [PubMed: 10037236]

[31]. Lin L, Song J, Song L, Ke K, Liu Y, Zhou Z, Shen Z, Li J, Yang Z, Tang W, Niu G, Yang H, Chen X, Simultaneous Fenton-like ion delivery and glutathione depletion by MnO2-based nanoagent to enhance chemodynamic therapy, Angew. Chem. Int. Ed 130 (2018) 4996–5000.

[32]. Ding B, Zheng P, Ma P, Lin J, Manganese oxide nanomaterials: synthesis, properties, and theranostic applications, Adv. Mater 32 (2020) 1905823.

[33]. Simonsen L, Viboud C, Mortality: a comprehensive look at the COVID-19 pandemic death toll, Elife 10 (2021), e71974. [PubMed: 34382937]

[34]. Kang Y, Sun C, Zhuang Z, Yuan R, Zheng Q, Li J, Zhou P, Chen X, Liu Z, Zhang X, Yu X, Kong X, Zhu Q, Zhong Q, Xu M, Zhong N, Zeng Y, Feng G, Ke C, Zhao J, Zeng M, Rapid development of SARS-CoV-2 spike protein receptor-binding domain self-assembled nanoparticle vaccine candidates, ACS Nano 15 (2021) 2738–2752. [PubMed: 33464829]

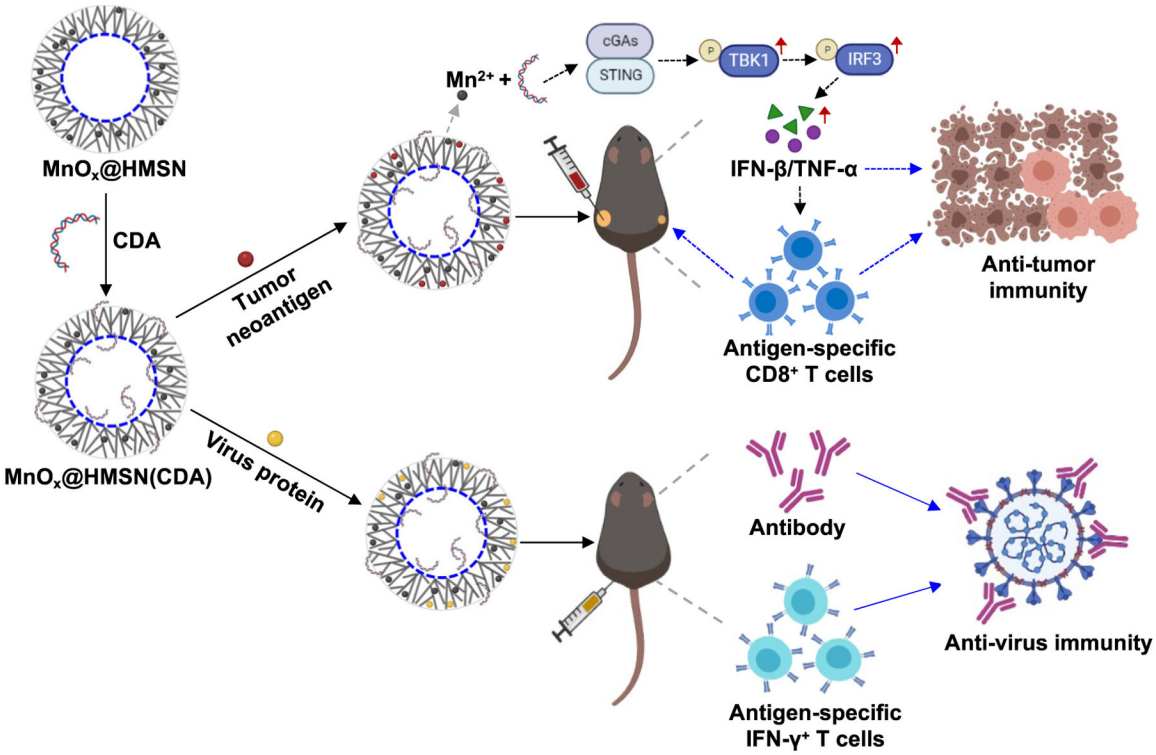

Fig. 1.

Schematic illustration of the MnO_x@HMSN(CDA) nanosystem. HMSN was synthesized by a water-oil biphase system, followed by a simple calcination process for coating small manganese oxide on the surface. STING agonist CDA and antigen peptides/proteins were loaded into the MnO_x@HMSN simultaneously by electrostatic and hydrophobic interactions. MnO_x@HMSN(CDA) loaded with tumor neoantigens elicited strong neoantigen-specific T-cell responses for cancer immunotherapy while MnO_x@HMSN(CDA) loaded with SARS-CoV-2 protein induce robust humoral and cellular immune responses against SARS-CoV-2.

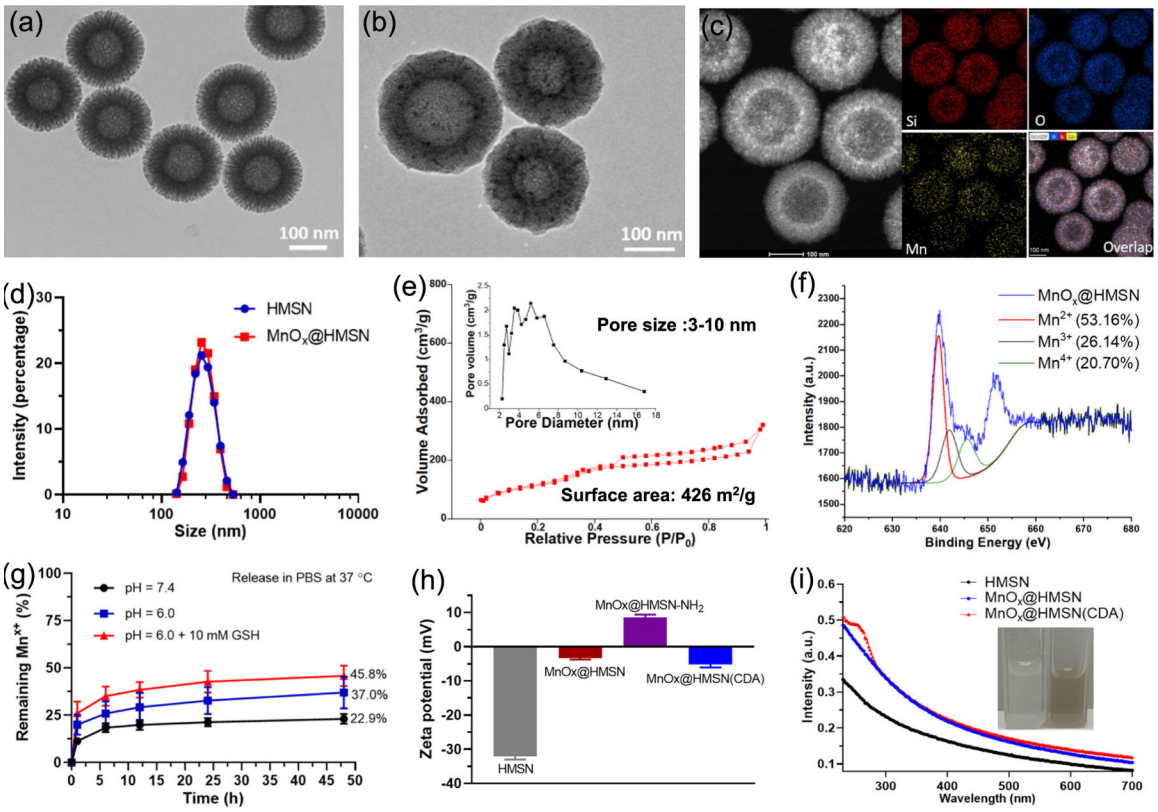

Fig. 2.

Material characterization of MnO_x@HMSN. TEM images of HMSN (a) and MnO_x@HMSN (b). (c) Elemental mapping of MnO_x@HMSN. (d) Size distribution of HMSN and MnO_x@HMSN by DLS. I Nitrogen adsorption and desorption isotherms and pore size distributions (inset) of MnO_x@HMSN. (f) X-ray Photoelectron Spectroscopy (XPS) results of MnO_x@HMSN. (g) Release of Mn ion in different pH of PBS with or without 10 mM GSH, as measured by ICP-MS. (h) Surface zeta potential of HMSN, MnO_x@HMSN, MnO_x@HMSN-NH2, and MnO_x@HMSN(CDA), as measured by Malvern Zetasizer. (i) UV–vis absorption spectra of HMSN, MnO_x@HMSN, and MnO_x@HMSN(CDA). The data show mean ± SEM from a representative experiment (n = 3 in (g) and (h)) from two independent experiments.

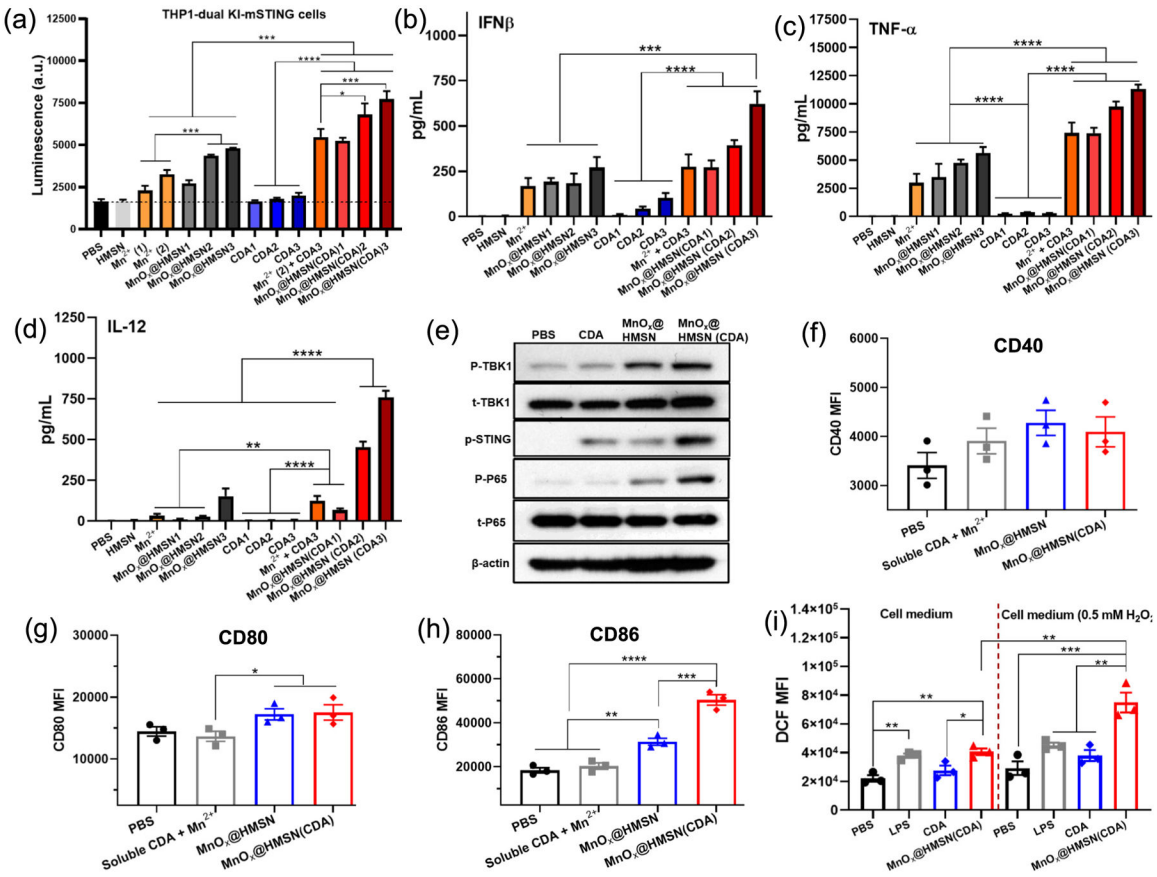

Fig. 3.

In vitro evaluation of STING activation and IFN-I response. (a) STING-IFN-I pathway activation in human monocyte-like THP-1 cells. (b-d) Cytokines secretion of IFN-β, TNF-α, and IL-12 from mouse BMDCs incubated with various formulations. The concentrations of CDA in CDA1/2/3 were 0.1/0.25/0.5 μg/mL, respectively. The concentrations of CDA and MnO_x@HMSN in MnO_x@HMSN(CDA1/2/3) were 0.1/0.25/0.5 μg/mL, and 15/30/60 μg/mL, respectively. (e) Western blot analysis of mouse BMDCs after incubation with either CDA (0.5 μg/mL), MnO_x@HMSN (60 μg/mL), or MnO_x@HMSN(CDA_0.5 μg/mL). (f-h) The mean fluorescence intensity (MFI) of CD40, CD80, and CD86 of BMDCs after incubation with either CDA (0.5 μg/mL) + Mn^{2+} (2.8 μg/mL), MnOx@HMSN (60 μg/mL), or MnO_x@HMSN (CDA_0.5 μg/mL) (i) The MFI of DCF in mouse BMDCs after incubation with LPS (0.5 μg/mL), CDA (0.5 μg/mL), or MnO_x@HMSN(CDA_0.5 μg/mL) with or without of 0.5 mM H_2O_2. The data show mean ± SEM from a representative experiment ($n = 3$) from two independent experiments. Data were analyzed by one-way ANOVA with Tukey's HSD multiple comparison *post hoc* test. $*P < 0.05$, $**P < 0.01$, $***P < 0.001$.

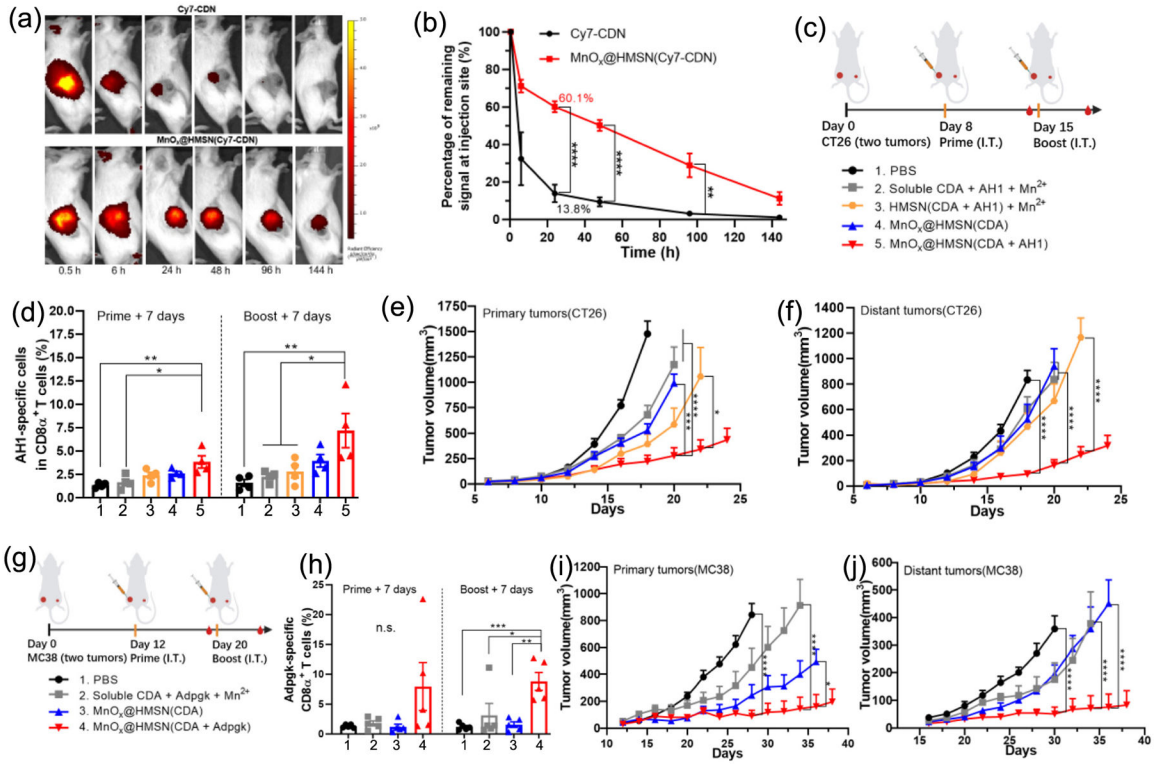

Fig. 4.

MnOx@HMSN(CDA) exhibits potent antitumor efficacy in CT26 and MC38 tumor models. (a) IVIS images of CT26 tumor-bearing mice administrated IT with free Cy7-CDN or MnO_x@HMSN(Cy7-CDN). (b) Percentages of remaining fluorescent signals at the injection site (compared to the signal at 0.5 h) at each time point. (c) Antitumor study design for the CT26 tumor model. (d) The frequencies of AH1-specific CD8α + T-cells among all CD8α + T-cells among PBMCs on days 15 and 22. (e-f) Growth of (e) primary and (f) distant tumors in the CT26 tumor model. (g) Antitumor study design for the MC38 tumor model. (h) The frequency of Adpgk-specific CD8α + T-cells among all CD8α + T-cells among PBMCs on days 19 and 27. (i-j) Growth of (i) primary and (j) distant tumors in the MC38 tumor model. The data show mean ± SEM from a representative experiment ($n = 3$ in (b); $n = 4$ in (c-f); $n = 5$ in (g-j)) from two independent experiments. Data were analyzed by one-way (d and h) or two-way ANOVA (b, e-f, i-j) with Tukey's HSD multiple comparison *post hoc* test. *$P < 0.05$, **$P < 0.01$, ***$P < 0.001$, ****$P < 0.0001$.

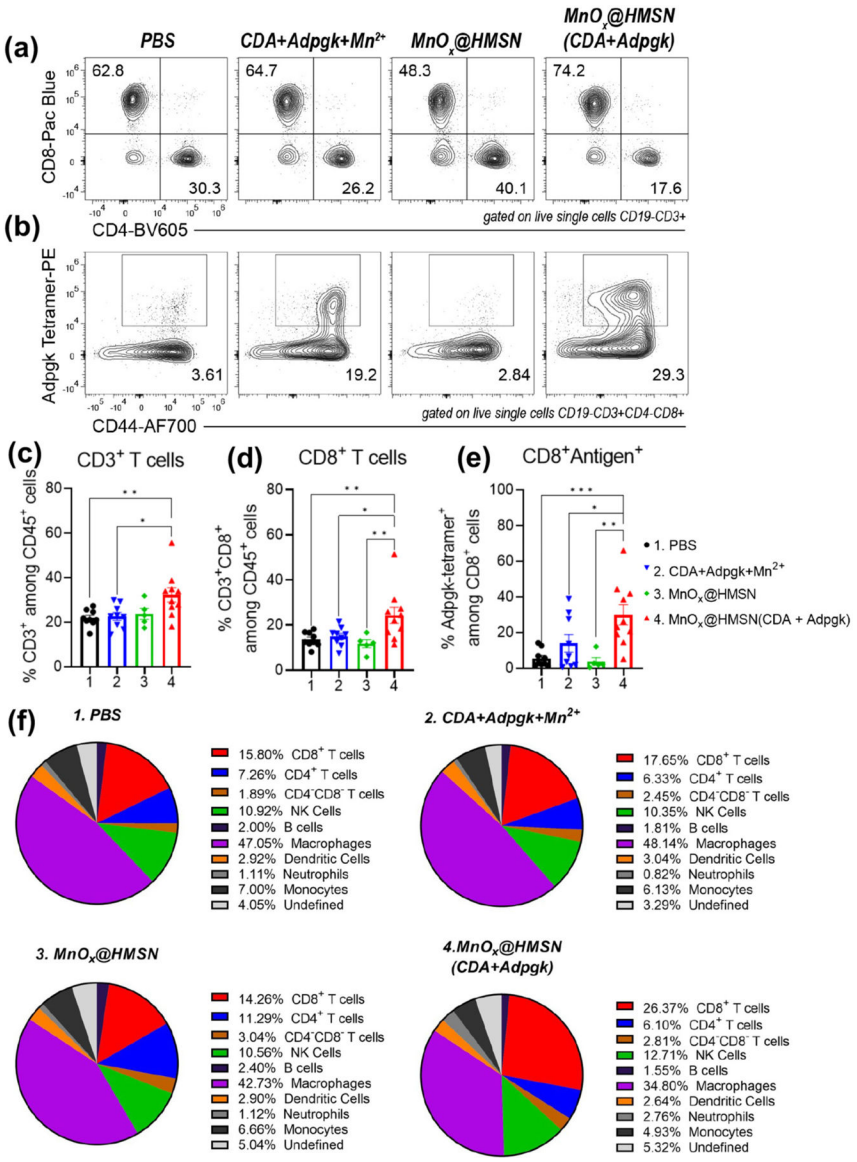

Fig. 5.

TME analysis after IT therapy with MnO_x@HMSN(CDA + Adpgk). (a-f) MC38 tumor-bearing mice were treated as in Fig. 4g and analyzed for intratumoral lymphocytes on day 27 (a) Representative flow cytometry scatter plots of $CD4^+$ and $CD8^+$ T-cells. (b) Representative flow cytometry scatter plots of neoantigen (Adpgk)-specific T-cells. (c-e) Intratumoral frequencies of (c) $CD3^+$ T-cells, (d) $CD8^+$ T-cells, (e) Adpgk-tetramer$^+$ $CD8^+$ T-cells. (f) Pie charts showing a summary of various cell types in the MC38 TME. Data represent mean ± SEM from a representative experiment ($n = 5$ for MnO_x@HMSN and $n = 9$ for other groups) from two independent experiments. Data were analyzed by one-way ANOVA with Tukey's HSD multiple comparison *post hoc* test. $^*P < 0.05$, $^{**}P < 0.01$, $^{***}P < 0.001$.

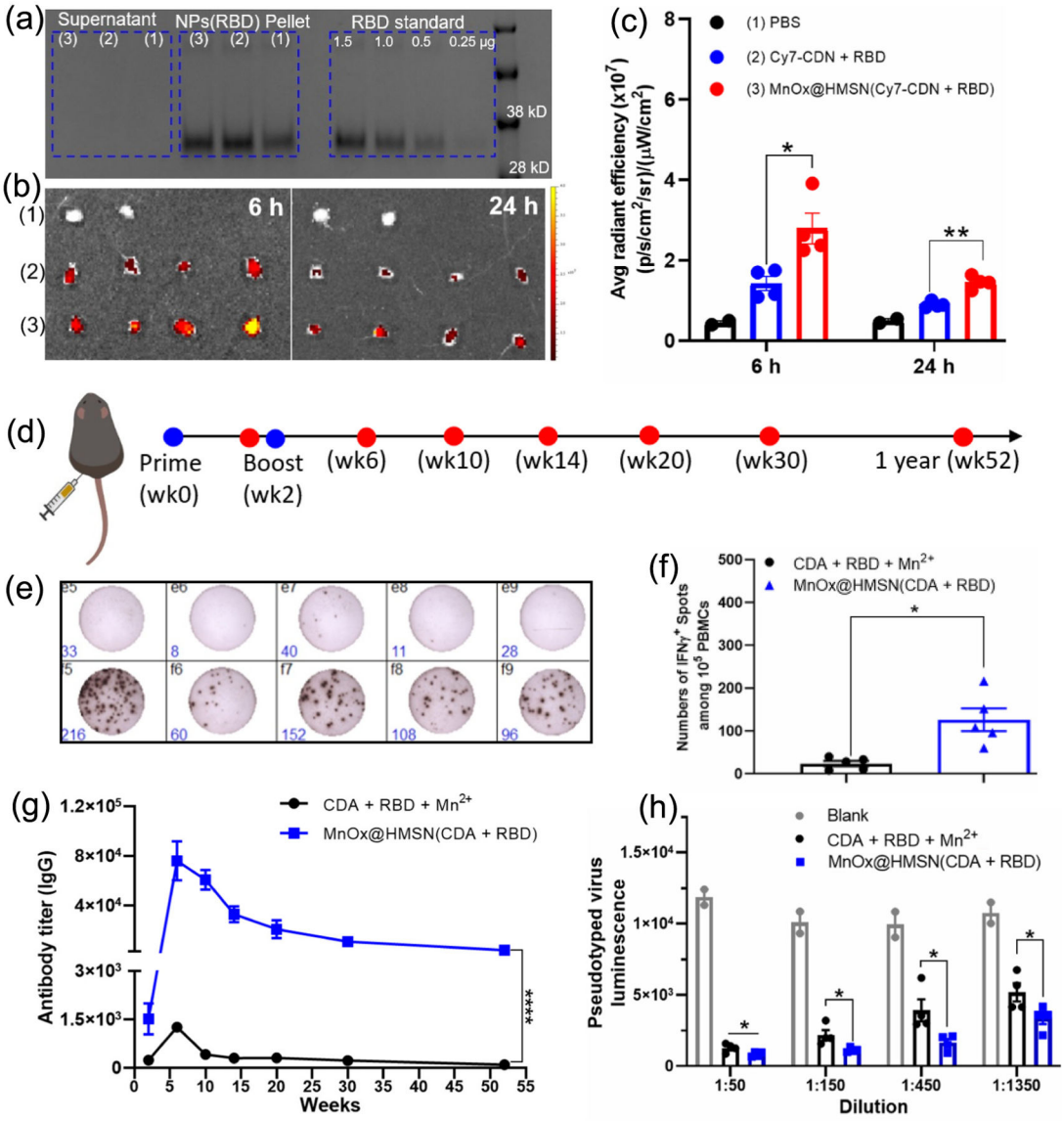

Fig. 6.

MnO_x@HMSN(CDA + RBD) as a vaccine platform against SARS-CoV-2. (a) MnOx@HMSN(CDA) was incubated with RBD protein for 30 mins at RT, followed by centrifugation (8000 *g*, 5 min) and SDS-PAGE analysis of pellet and supernatant for RBD. (b) IVIS images of inguinal lymph nodes after 6 h or 24 h of SC administration with (1) PBS, (2) Cy7-CDN + RBD, or (3) MnO_x@HMSN(Cy7-CDN + RBD). (c) Quantification of average fluorescence intensity in inguinal lymph nodes. (d) Vaccine study design with MnO_x@HMSN(CDA + RBD). (e-f) IFN-γ ELISPOT assay of SARS-CoV-2 RBD protein-specific T-cell response using mouse PBMCs harvested on week 4. (g) Humoral RBD protein-specific IgG serum titer at various time points. (h) *In vitro* pseudo-typed virus neutralization assay using mouse sera harvested on week 6. The data show mean ± SEM with $n = 4$ in (c, h) and $n = 5$ in (f-g). Data were analyzed by one-way (c, f, h) or two-way

(g) ANOVA with Tukey's HSD multiple comparison *post hoc* test. *$P < 0.05$, **$P < 0.01$, ***$P < 0.001$, ****$P < 0.0001$.